Research article

Spectral Induced Polarization Response of Clay Rock Samples with a High Value of Pyrite

Saeide Ahmadi[1]*, Ahmad Ghorbani[1]

1- Dept. of Mining and Metallurgy Engineering, Yazd University, Yazd, Iran

*Corresponding author: E-mail: *saeedeahmadi120@gmail.com*

Keywords	Abstract
Black Shales **Chargeability** **Time Constant** **High-Grade** **Sulfides**	The induced polarization (IP) response in media containing clay and/or metallic minerals has been modeled in different research. Increasing the IP applications and measurements has revealed these models' limitations. For instance, no model has described IP response in the media with metallic minerals higher than 22 percent. So, our goal in this contribution is to explain the IP response of clay-rich samples containing low- to high-grade pyrite, galena,

and sphalerite from the Zn-Pb sedimentary-exhalative mine Koushk, central Iran. The samples' background consists of clayey/micaceous minerals, including illite, muscovite, and chlorite, that, along with the metallic minerals, make the consecutive layers in some samples, while others have a different formation. The samples also contain some insulating grains such as quartz and gypsum. Therefore, there are different conduction and polarization mechanisms in them. These properties make our samples unique and substantial to study the IP response. To do this, we measured the samples' complex conductivity, density, porosity, cation exchange capacity (CEC), and metallic/non-metallic minerals. Then, we investigated the relationship between electrical and petrophysical properties. The results showed that the chargeability has no relationship with CEC and is a complete representation of the metallic minerals' polarization. The normalized chargeability depends linearly on the quadrature conductivity and is affected by the metallic minerals besides CEC. The content and type of clay/mica minerals control the CEC. Hence, the normalized chargeability is influenced by the metallic and non-metallic polarizable components. The conductivity linearly relates to metallic minerals' content and, in vein mineralizations, has higher values than disseminated ones. Ultimately, comparing our samples' IP response with Revil et al.'s and Pelton et al.'s models for chargeability, metallic minerals volume content, and time constant determined that increasing the metallic minerals makes the chargeability decrease and the time constant increase. So, in high-grade porous media or non-dispersive formations, chargeability is a function of the metallic minerals' volume content and the time constant. Complex media like our samples are expected in geological environments. Hence, recognizing the parameters affecting IP response in these media helps to better understand their properties and, in general, IP response characteristics.

1. INTRODUCTION

The non-invasive geophysical induced polarization (IP) method is the science of studying reversible charge carriers around grains in porous media. Based on the strong IP response of metal particles, the method has been used in the mining industry for metallic deposit exploration [1-5]. IP is also utilized widely in environmental studies such as contaminant delineation [6-8], contaminant remediation monitoring [9-12],

bioremediation of contaminants [13-14], monitoring of tailing dams and mine drainage [15-16], long-term storage of nuclear wastes [17], likewise, geothermal and volcanology studies [18-20], cement improvement [21-23], geotechnical investigations [24], hydrocarbon exploration [25-28], petrophysical studies [29-38], identifying of clays properties [39-41], and hydrogeophysics [42,43].

Many IP models have been constructed so far to understand better the parameters affecting the IP response, such as [44-68]. Amidst, the relationship between metallic minerals content and IP response has been researched since the innovation of the IP method by Schlumberger in 1920 [69]. This research focused on the relationship between the magnitude of IP response and petrophysical properties in the disseminated or the low volume content (mainly less than 16%, e.g., [49]) materials. As a result, Revil et al. (2015a) disclosed the first quantitative model that relates the chargeability and volume content of metallic minerals for disseminated mineralization with a grade of up to 22% [66]. However, the proposed IP models do not appropriately fit the experimental data in high-grade non-disseminated mineralization. In other words, to our knowledge, there is no model to describe the IP response in media with metallic minerals content higher than 22 %. So, in the present article, we will study the electrical responses in high-grade dispersed to layered samples. In particular, we will focus on the relationship between the samples' chargeability and metallic mineral volume content.

To achieve this, we collected mineralized clay-rich dark shale samples from Zn-Pb mine Koushk (K-samples), central Iran. Then, complex conductivity measurements were conducted on them in the frequency range of 10 millihertz (mHz) to 45 kilohertz (kHz) in pore-water conductivity of 0.36 S/m. Afterward, the IP parameters, including in-phase and quadrature conductivities at specific frequencies, chargeability, normalized chargeability, time constant, and conductivity itself, were extracted from the raw data. Meanwhile, metallic (including pyrite, galena, and sphalerite) and non-metallic minerals (e.g., clays, micas, and organic matter) content were determined by the semi-quantitative X-ray diffraction (XRD) method. Also, the thin and polished sections of the samples were prepared and studied. The K-samples' porosity, density, and cation exchange capacity (CEC) were measured, as well. Eventually, we analyzed the relationship between the petrophysical quantities and IP parameters.

2. THE STUDY AREA

The Koushk Zn-Pb mine is one of the largest sedimentary-exhalative (SEDEX) deposits in the Zarigan-Chahmir basin, central Iran [70-71] (Fig. 1). The deposit is located about 167 km east of the city of Yazd at 31°40'N and 55°40'E.

According to the lithologic characteristics, there are two sequences of rock units in the mine area, including the mine and volcano-sedimentary sequences. The mine sequence consists of rhyolites, calcareous sandstone, silt, barren and mineralized black shale, limestone, and dolomite. The volcano-sedimentary sequence includes volcanic tuffs, limestone, dolomite, microconglomerate, and two hematite horizons. The age of black shale, the main rock unit in the area and host to the ore minerals, is upper proterozoic. This unit has very fine laminations. Quartz grains, clay minerals, and organic matter are also observed in the unit [72].

The ore minerals in the mine include sphalerite (ZnS), galena (PbS), and melnicovite (a mixture of marcasite (FeS_2) and pyrite (FeS_2)). The gangue minerals are pyrite, quartz, calcite, dolomite, gypsum, anhydrite, and clays. Variscite, a green mineral of hydrated aluminum phosphate ($AlPO_4.2H_2O$), is also reported in the deposit. Minerals in the Koushk mine have a variety of structures and textures, including laminated, disseminated, massive type, brecciated, frameboidal, and botryoidal [72].

Pyrite and galena, among other minerals, were crystallized in more than one crystallization stage. In the first stage, euhedral-shaped pyrite was formed, common in the shale but less common in the mineralized zones. Xenomorphic pyrites in spherical shape were produced in the second stage. Pyrite with a skeletal texture is the result of the third stage. The size of pyrite grains varies from a few microns to a few millimeters [72].

Euhedral and xenomorphic galena have appeared in the first and second stages of galena crystallization, respectively. Galena mineralization has followed the sphalerite mineralization [72].

The main alterations in the Koushk deposit are carbonatization and sericitization [73].
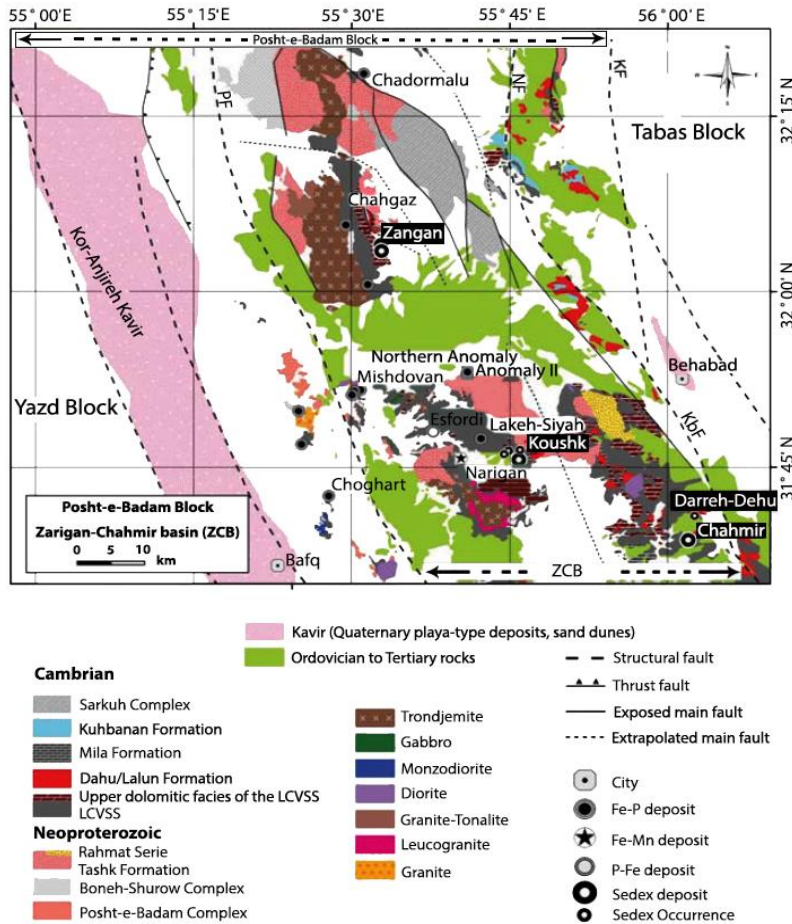
Fig. 1. A simplified geological map of the Zarigan–Chahmir basin that shows the location of SEDEX deposits within the basin. KbF, Kuhbanan Fault; KF, Kalmard Fault; NF, Naeini Fault; PF, Posht-e-Badam Fault [73].

3. METHODOLOGY

The eight samples of this study, i.e., K6, K12, K17, K18, K19, K20, K23, and K26, are shown in Fig. 2. We wrote the minerals' names that can be seen in the macroscopic view in this figure. Also, we drew the white dashed lines as guides to the eyes to separate the clay/mica and metallic layers. The lengths of the samples are between 6.8 and 12.4 cm. The samples K6 and K19 were unintentionally broken into two pieces before the complex conductivity measurements. However, we used one part of each sample for the measurements (i.e., K6a and K19b, considered K6 and K19 in the following). All the samples have a layered structure besides the disseminated one. The samples K20 and K26 differ from the others (Fig. 2).

3.1. Chemical Analyses

The metallic minerals weight content of the samples was determined via the semi-quantitative XRD method. Then, we computed the volume content of metallic minerals in each sample utilizing the metallic minerals' weight content,

densities of the metallic minerals, and total sample density (Table 1). Accordingly, the metallic minerals volume content of the samples varies between 0.062 and 0.533.

The weight percentage of clay/mica minerals in the samples, including muscovite, illite, and chlorite, was also obtained through the semi-quantitative XRD method (Table 1).

The highest values of clayey and micaceous minerals belong to K6, K18, K12, K17, and K23 (26 to 17 percent). The lowest values of these sheet minerals are observed in K26, K20, and K19 (zero to 9 percent).

The main mineral in sample K26 is variscite (80 percent, as seen in Table 1).

K-samples' organic matter was calculated using the Loss of ignition (L.O.I.) method from [74] (see also [75-76]). Accordingly, the organic matter of the samples varies from 0 to 0.282 % (Table 1).

3.2. Other Characteristics Of The Samples

We reported the density, porosity, and CEC of the samples in Table 2. The samples were saturated with a low-salinity NaCl solution in a vacuum chamber for 24 hours to measure the porosity. Then, the water content was reduced to the

porosity (see, for instance, [77]). The density was determined by measuring the samples dry and water-saturated weights and volumes.

CEC was determined by using a hexammine cobalt (III) chloride solution from the Ciesielski and Sterckeman (1997) method [78]. We reported CEC in the traditional unit meq/100gr (= 963.20 C/kg in S.I. units).

CEC corresponds to the exchangeable cations on the surface of the clay minerals per unit mass of minerals [77]. In other words, CEC represents the total amount of cations that can be sorbed on the surface of clay minerals [79]. Cobalt ions can be intensely exchanged with the surface reactive cations of clay minerals. Accordingly, each sample was crushed and sieved in our measurements to achieve a size fraction between 150 and 425 μm. Then, fine-grain clays were added to a 0.05 N hexammine cobalt solution with an orange color.

As a result, the color of the solution got weaker due to the sorption of cobalt ions on the surface of clay minerals. This color reduction obtains the hexammine cobalt (III) chloride quantity used in the sorption procedure. The difference in cobalt ions concentration of the solution before and after contact with clay minerals was measured through absorbance measurements with a calibrated spectrophotometer. The difference determines the concentration of exchangeable cations of clay minerals, i.e., CEC [18,80-81]. The importance of CEC in geophysics is to obtain the surface conductivity of clay minerals by using their CEC.

Based on these methods, samples K18 and K20 contain the highest and lowest porosity values. K20 and K23 have the most and the least density. The highest and lowest values of CEC belong to K23 and K26.

Fig. 2. Picture of eight (without K6b and K19a (see the main text)) mineralized dark clay rock samples from Zn-Pb Koushk mine. The samples have a relatively low porosity. Metallic minerals are found as interlayers within the shale background. All the samples have a layered structure besides the disseminated one. K20 and K26 differ from the others. White areas in K20 consist of gypsum. Green particles in K26 are Variscite. White dashed lines highlight the traces of shale and metallic layers. Shale (sh), organic matter (om), gypsum (g), pyrite (py), galena (ga), sphalerite (sph), and variscite are annotated.

Table 1. The metallic and non-metallic minerals in K-samples. The metallic minerals' weight content was determined using the semi-quantitative XRD method. The metallic minerals' volume content is calculated by the metallic minerals' weight content, densities of metallic minerals, and total sample density. We displayed the lack of sphalerite, galena, and variscite in some samples with a star (*). Organic matter in K12, K17, and K23 is undefined due to the inadequate amount of these samples.

|	Sample	K6	K12	K17	K18	K19	K20	K23	K26
Weight content	Sphalerite (%)	11	5	2	1	*	24	17	6
	Pyrite (%)	15	21	27	13	57	16	4	3
	Galena (%)	*	*	*	*	*	21	2	*
	Metallic minerals (%)	26	26	29	14	57	61	23	9
Volume content	Sphalerite (%)	8.003	3.411	1.385	0.667	*	26.426	10.316	4.424
	Pyrite (%)	8.940	11.737	15.321	7.098	42.636	14.432	1.988	1.812
	Galena (%)	*	*	*	*	*	12.462	0.654	*
	Metallic minerals (%)	16.943	15.148	16.707	7.765	42.636	53.320	12.959	6.236
	Metallic minerals (-)	0.169	0.151	0.167	0.078	0.426	0.533	0.130	0.062
Clay/ mica	Muscovite, Illite (%)	22	18	17	21	5	1	17	0
	Chlorite (%)	4	3	3	5	4	1	0	0
	Organic matter (%)	0.025	undefined	undefined	0.056	0.008	0	undefined	0.282
	Variscite (%)	*	*	*	*	*	*	*	80

Table 2. Characteristics of the K-samples. The density was determined by measuring the samples' dry and water-saturated weights and volumes. The porosity was computed thanks to the water content of the samples. CEC, in meq/100 gr (= 963.20 C/kg), was calculated by the hexammine cobalt method.

Sample	Density (g/cm³)	Porosity (-)	CEC (meq/100gr)
K6	2.98	0.04	5.54
K12	2.79	0.03	9.62
K17	2.84	0.03	8.30
K18	2.73	0.09	11.80
K19	3.74	0.06	4.4
K20	4.51	0.02	2.55
K23	2.49	0.06	13.70
K26	3.02	0.07	1.45

3.3. Mineralogical Studies

We chose K6, K19, K20, and K26, two-layered and two non-layered K-samples, to observe the metallic and non-metallic minerals assemblage. Therefore, we prepared and analyzed the polished sections of K6, K19, K20, and K26 and the thin section of K6 in the thin section laboratory of Yazd University (Fig. 3). The results showed that K6 consists of a layered structure of metallic and non-metallic minerals, including pyrite, sphalerite, galena, gypsum, quartz, oriented sericite particles, shale, and organic matter. Sericite is the white micas with fine, ragged grains and aggregates commonly made from muscovite, illite, or paragonite.

K19 includes pyrite in between the layers of non-metallic gangue. Pyrite, sphalerite, galena, and non-metallic gangue are observed in K20, which has no layered structure. Variscite, pyrite, and non-metallic gangue exist in K26. K26 has low metallic particles dispersed within the variscite background.
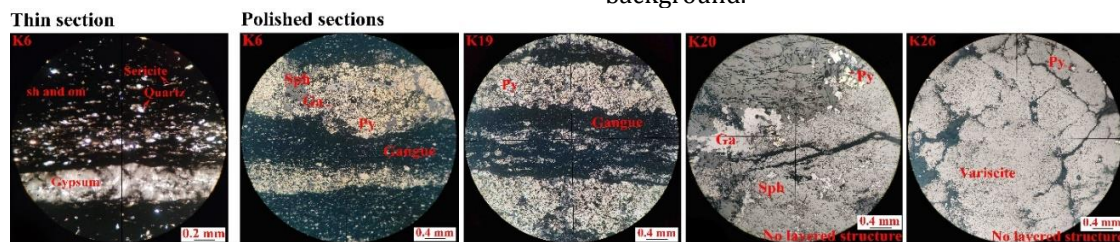
Fig. 3. The thin section of K6 and the polished sections of K6, K19, K20, and K26. K6 contains pyrite (Py), sphalerite (Sph), galena (Ga), gypsum, quartz, oriented sericite particles, shale (sh), and organic matter (om). K19 includes pyrite placed in non-metallic gangue. K20 consists of pyrite, sphalerite, galena, and non-metallic gangue. Variscite, pyrite, and non-metallic gangue exist in K26. The layered structure of metallic minerals and non-metallic gangue are apparent in K6 and K19. K20 and K26 have different structures.

3.4. Complex Conductivity Measurements

The complex electrical impedance measurements $(Z^*(\omega)=|Z^*(\omega)|e^{i\varphi})$ were conducted using a four electrodes technique (see, for instance, [82-84]) and the high-precision impedance analyzer developed by Zimmermann et al. [84]. The four electrodes technique utilizes two superconductive carbon films as current electrodes (A and B), two non-polarizing Ag-AgCl Biomedical electrodes as voltage electrodes (M and N), and a sample holder. The current electrodes were placed at two reciprocal end faces of each sample. The voltage electrodes were placed on one side of the sample in the middle of the current electrodes. The current electrodes covered all the end faces of the sample. Conversely, the voltage electrodes had a small surface (see, for instance, [8,77,83,85]) (Fig. 4).

The impedance amplitude ($|Z^*(\omega)|$ in Ω) and the phase angle (φ in rad) were measured at the frequency range from 10 mHz to 45 kHz. Then, the amplitude and the phase were used to calculate the in-phase (σ' in S/m) and quadrature (σ'' in S/m) conductivity (Fig. 5) through Eq. (1-8):

$$Z^*(\omega)=Z'+iZ'', \text{ in } \Omega, \quad i=\sqrt{-1} \tag{1}$$

$$Z'=\text{Re}(Z^*(\omega))=|Z^*(\omega)|\cos\varphi, \text{ in } \Omega \tag{2}$$

$$Z''=\text{Im}(Z^*(\omega))=|Z^*(\omega)|\sin\varphi, \text{ in } \Omega \tag{3}$$

$$G'=Z'/|Z^*(\omega)|^2, \text{ in S} \tag{4}$$

$$G''=-Z''/|Z^*(\omega)|^2, \text{ in S} \tag{5}$$

$$\sigma'=G'k, \text{ in S/m} \tag{6}$$

$$\sigma''=G''k, \text{ in S/m} \tag{7}$$

$$k=MN/\frac{\text{Samples' cross-sectional area,}}{\text{in 1/m}} \tag{8}$$

where ω is the angular frequency in rad/s. The geometric factor (k) used in the calculations was different for the samples due to their different MN distance and samples' cross-sectional area. The imposed injection voltage for the measurements was 1 V.

The electrolyte conductivity in the measurements was 0.36 S/m. So that before the measurements, a brine was prepared with demineralized water and a high-grade dehydrated NaCl salt at 25°C. Then, the samples were put in a closed container for two weeks in the brine, and their conductivity was measured until it was stabilized. Then, the samples were removed from their containers for the measurements (see, for instance, [77]).

The measurements were performed in four quadrupoles to study the IP response anisotropy. The current passes the sample parallel to the bedding plane of shale and metallic minerals in quadrupoles 1 and 2 and perpendicular to it in quadrupoles 3 and 4 (Fig. 4). We will discuss the IP response anisotropy in our future study. However, see [86] for the initial results. The present paper considers complex conductivity measurements in the case of quadrupole 3. This is because the number of IP parameters we could extract from in-phase and quadrature conductivity spectra in this quadrupole was more than in the others.
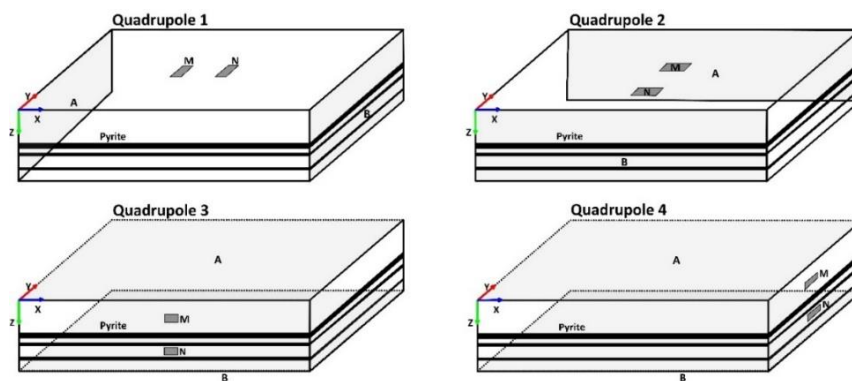

Fig. 4. Four-electrode configurations on a cubic sample for the spectral induced polarization (SIP) measurements. The current (A, B) and voltage electrodes (M, N) were placed on the different sides of the samples. The current electrodes covered all the reciprocal end faces of each sample (light-gray planes), but the voltage electrodes had a small surface (small dark-gray planes). The current electrodes were superconductive carbon films. The voltage electrodes were non-polarizing Ag-AgCl Biomedical electrodes. Current passes the sample parallel to the bedding in quadrupoles 1 and 2 and perpendicular to it in quadrupoles 3 and 4. This paper finds measurements in the case of quadrupole 3.

4. THEORY

The polarization phenomena studied using the IP method are described as a contribution of conductivity (σ). The conductivity is complex owing to polarization phenomena and frequency-dependent due to relaxation processes [87]. Complex conductivity (σ*(ω) in S/m) is written as:

$$\sigma^*(\omega)=(1/kZ^*(\omega))=\left|\sigma^*(\omega)\right|e^{-i\varphi} \qquad (9)$$
$$=\sigma'(\omega)+i\sigma''(\omega)$$

$$\left|\sigma^*(\omega)\right|=\sqrt{(\sigma'(\omega))^2+(\sigma''(\omega))^2} \qquad (10)$$

where $\left|\sigma^*(\omega)\right|$ is the complex conductivity amplitude in S/m. The in-phase conductivity shows transporting the electric charge carriers, i.e., the perfect conduction. The quadrature conductivity corresponds to the reversible storage of electric charge carriers [18,88], i.e., the perfect polarization. The phase difference between the applied external electric field and the resultant voltage in the IP method is determined with:

$$\varphi=\arctan(\sigma''(\omega)/\sigma'(\omega)) \qquad (11)$$

There are distinct polarization mechanisms in porous media containing polarizable metallic and non-metallic materials, like K-samples. Immediately after applying the external electric field, the charge carriers on the surface of the polarizable materials go into motion. This movement results in a maximum conductivity limit as high-frequency or instantaneous conductivity ($\sigma=\sigma_\infty$, in S/m). After a long-term applied external electric field, the opposite-sign charge carriers are separated in two sides of the polarizable grains. They cannot participate in the conductivity of the porous media as before. So, low-frequency or DC conductivity is formed ($\sigma=\sigma_0$, in S/m). Chargeability (M, dimensionless) is calculated by the ratio of these conductivities [89]:

$$M=(\sigma_\infty-\sigma_0)/\sigma_\infty \qquad (12)$$

Normalized chargeability (in S/m) is given by [66,90]:

$$M_n=M\sigma_\infty=\sigma_\infty-\sigma_0 \qquad (13)$$

Revil et al. (2015a) have derived σ_∞ and σ_0 using the Maxwell-Clausius-Massotti equation and the differential effective medium approach:

$$\sigma_\infty=\sigma_b^*(1+3\varphi_m) \qquad (14)$$

$$\sigma_0=\sigma_b^*(1-(3/2)\varphi_m) \qquad (15)$$

where σ_b^* is the background conductivity containing polarizable materials and φ_m (dimensionless) is the volumetric content of metallic minerals.

Hence, the chargeability can be written in the following equation for metallic minerals volume content smaller than 22% of the whole materials, as exposed in [66,91]:

$$M=(9/2)\varphi_m \qquad (16)$$

Metallic minerals refer to metals (such as lead, silver, and copper), semiconductors (such as pyrite and magnetite), and semi-metals (such as graphite) [19,82,92]. The metallic minerals in this paper denote the semiconductors, i.e., pyrite, galena, and sphalerite. The background material is part of the porous media composed of non-metallic particles, like sand, clays, and pore water.

When the background is polarizable, Eq. (16) is rewritten into [66]:

$$M=(9/2)\varphi_m+M_b \qquad (17)$$

M_b is the background chargeability, less than 10% [93-99].

The last IP parameter to introduce here is the main time constant (τ in s) that for the complex conductivity is written as [46,66]:

$$\tau=a^2/D \qquad (18)$$

where a is the radius of the metallic particles (in m), and D (m²/s) is the apparent diffusion coefficient of the charge carriers responsible for the polarization of the conductive particles. τ is determined from the peak frequency of the phase angle spectrum ($\tau=1/2\pi f_{peak}$).

We took the K-samples' instantaneous conductivity, chargeability, and time constant from the double Cole-Cole model (Appendix A).

5. RESULTS

5.1. The Characteristics Of The Background Materials

Fig. 5 represents the in-phase and quadrature conductivity spectra for K-samples. We fitted a double Cole-Cole model in conductivity form to the spectra to extract the Cole-Cole parameters of K-samples. Then, we reported the parameters, including σ_∞, M, c, and τ in low- and high-frequency in Table 3. Parameter c is the Cole-Cole exponent (dimensionless) and has a reverse relationship with the particle size distribution of the metallic particles. c, which varies between 0 and 1, is the slope of the phase angle log-log

symmetric spectrum [100-101]. Samples K20 and K23 are not displayed/reported in Fig. 5 and Table

3 because the Cole-Cole model did not fit well on their conductivity spectra.
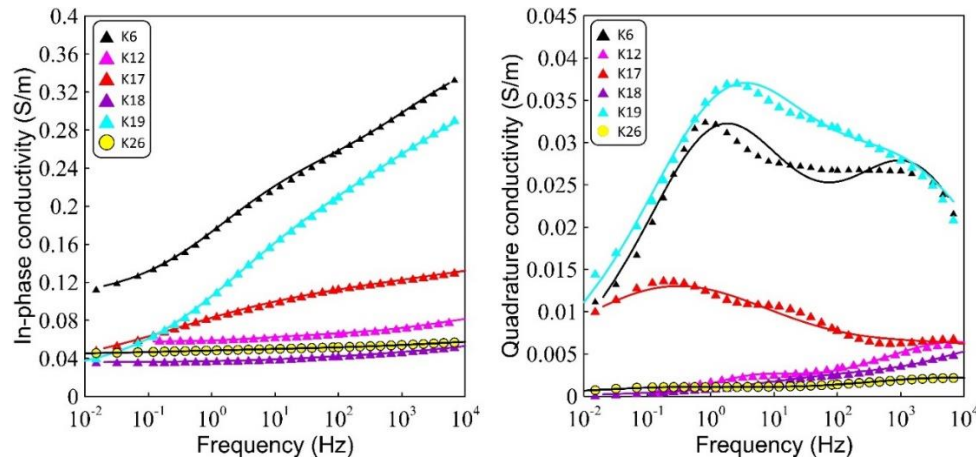

Fig. 5. K-samples' in-phase and quadrature conductivity spectra (at a pore-water conductivity of 0.36 S/m). We eliminated the high-frequency part of the spectra (10-45 kHz), diminishing unintended errors. The lines represent the double Cole-Cole model in conductivity form. K20 and K23 are not displayed in this figure because the Cole-Cole model did not fit well on their spectra.

Table 3. Double Cole-Cole parameters for K-samples. The parameters of K20 and K23 are not reported in this table because the Cole-Cole model did not fit well on their spectra. LF and HF state low- and high-frequency Cole-Cole parameters, respectively.

Sample	σ_∞ (S/m)	M1 (LF)	M2 (HF)	c1 (LF)	c2 (HF)	$\tau 1$ (LF)	$\tau 2$ (HF)	rms (%)
K6	0.36944	0.41055	0.31510	0.47758	0.50197	0.1192850	0.0000973	0.28672
K12	0.09789	0.05706	0.35430	0.73108	0.45174	0.0305207	0.0000202	0.57357
K17	0.15571	0.59087	0.25697	0.33657	0.31178	0.6511714	0.0000105	0.35869
K18	0.06947	0.19788	0.28719	0.39485	0.59009	0.0010632	0.0000043	0.28733
K19	0.33673	0.55624	0.38001	0.42258	0.41021	0.0830001	0.0000935	0.22838
K26	0.06380	0.09440	0.21260	0.38978	0.38777	0.6086066	0.0000236	0.14126

As mentioned in the SIP literature, the highly accurate part of complex conductivity spectra is from 10 mHz to 1 kHz [62,84,102]. It is observed that the kHz range of SIP errors rises from the unintended capacitive coupling in the SIP measurement set [32,36,103-105], and mHz range errors are caused by electrochemical effects [65]. It is also observed that when the background conductivity is very high, SIP measurement error increases [106]. So, in the present study, we considered SIP data in the frequency range of 1 Hz to 1 kHz to eliminate the uncertainties in measurement data by very low and high frequencies. Moreover, to evaluate the precision of the measurements, we repeated them three times at each frequency and observed good repeatability in our measurements.

The analyses show that there are various amounts of clayey and organic matter in K-samples (Table 2). CEC is a parameter mostly related to the clay type (e.g., smectite, illite, kaolinite) and the clay minerals' weight fraction

[76,107]. In the same way, we observed a linear relationship between CEC and clay/mica weight fraction for our samples and data from the literature [10,108] (Fig. 6).
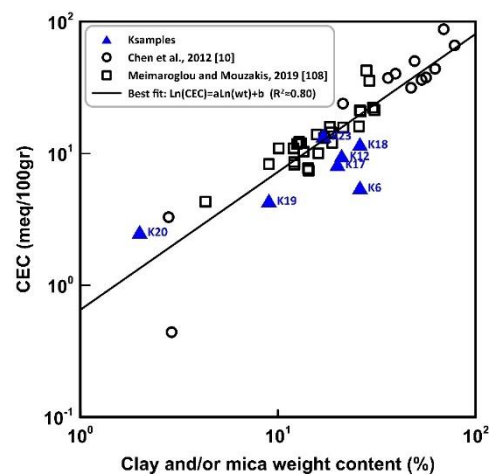

Fig. 6. The linear relationship between CEC and clay/mica weight fraction for K-samples and data from the literature. K26 is not shown in this figure due to no clay/mica content.

We calculated the normalized chargeability for K-samples using the Cole-Cole model ($M1\sigma_\infty$) and for some literature from their reported values for instantaneous conductivity and chargeability (Eq. 13). Then, we displayed the CEC versus the normalized chargeability and chargeability in Fig. 7a and Fig. 7b, respectively. Accordingly, the normalized chargeability versus CEC can be fitted with a straight line, especially for the data from the literature (see [95,109-110] as well). Compared with the literature's data, K-samples are rich in metallic minerals. So, we investigated the relationship between the normalized chargeability and the metallic minerals' volume content (Fig. 8). We found a good correlation between these two parameters. The normalized chargeability for K-samples with high-value metallic minerals is higher than the others. So, we can probably attribute the different K-samples' CEC-normalized chargeability behavior in Fig. 7a to their higher metallic minerals content than the literature's data. Such behavior has also been observed by Revil et al. (2018d). It seems these observations reveal that the normalized chargeability depends on the metallic minerals content besides the CEC (see also [96,98]). K12 does not follow this concept (Figs. 7a and 8). We attribute it to a weaker Cole-Cole fit with more rms than the other K-samples (Table 3), causing its normalized chargeability to be a little problematic.

Conversely, there is no relationship between chargeability and CEC (Fig. 7b). This implies that the factors controlling CEC, such as clay's content and type, do not impact the chargeability. This result is substantial, particularly in our samples with different polarization mechanisms due to the simultaneous presence of clay/mica, metallic minerals, insulator grains, and pore water.

The data shown in Fig. 9 exhibit a linear trend with a slope of 5.12 between the normalized chargeability and the quadrature conductivity (see also [79,85,92,109-111]). We determined the latter for the K-samples at the geometric mean frequency [111] of 10 Hz. So, the K-samples' normalized chargeability is approximately five times higher than the quadrature conductivity. The literature's data in Fig. 9 are the volcanic samples mainly containing clayey materials. Notably, the normalized chargeability is linearly connected to the quadrature conductivity in the samples with or without metallic content. The normalized chargeability and quadrature conductivity of K-samples are even higher than those for pure bentonite and pure kaolinite (95 and 80 percent, respectively, from [112]).

The linear relationship between the normalized chargeability and the quadrature conductivity emphasizes that the observations between the normalized chargeability and CEC are also valid for the quadrature conductivity [85] (Fig. 10). Hence, background polarizable materials, like clay/mica fraction, control the CEC, normalized chargeability, and quadrature conductivity [20,110]. The metallic content can also affect these two IP parameters. Nelson and Van Voorhis (1983) have also reported a direct correlation between the quadrature conductivity and the metallic minerals content [113].

The normalized chargeability as a conductivity function is presented for K-samples and data from the literature in Fig. 11. We calculated K-samples' conductivity using in-phase and quadrature conductivity at 10 Hz (Eq. 10). Based on Eq. (17), the chargeability is considered under the control of the background chargeability and the metallic minerals' volume content. In turn, the background chargeability (M_b) can be obtained by Eq. (13) ($M_b = M_n^b/\sigma_\infty^b$). At low pore-water salinity, in which the surface conductivity dominates the pore-water conductivity, the background chargeability has a maximum limit (R) of around 0.1. In this state, the overall conductivity of materials is defined by the surface conductivity ($\sigma = \sigma_\infty^b = \sigma_s^\infty$) [77,79,90]. All minerals, including clays, organic matter, and semiconductors, have surface conductivity when in contact with water [88]. The K-samples have three conductivity mechanisms: electrolyte, surface, and semiconductor. The placement of K-samples above the line $M_n = 0.1\sigma$ in Fig. 11 shows that the surface conductivity is very high among these different mechanisms and is the dominant conductivity component in the K-samples (see, for instance, [77,98]). We represented the smectite- and magnetite-rich samples from the literature [77,90] along with the lines $M_n = 0.4\sigma$ and $M_n = 0.6\sigma$ to compare with the K-samples location. The lines $M_n = 0.4\sigma$ and $M_n = 0.6\sigma$ were plotted following the highest amounts of K-samples chargeability, i.e., 0.59, 0.56, and 0.41 for K17, K19, and K6, respectively. K-samples are located even higher than smectite-rich soils. We believe these observations demonstrate the influence of the metallic minerals content on the conductivity (besides the normalized chargeability).

So, we analyzed the relationship between the conductivity and the metallic minerals weight content either for K-samples or disseminated/vein mineralizations originating from [114] (redrawn from [113]) (Fig. 12). As is seen in Fig. 12, these two parameters are linearly related. K-samples also have high-value conductivity that is comparable with vein mineralization. Hence, the metallic minerals, besides the background conductive materials, are essential in increasing K-samples' overall

conductivity. We can attribute this behavior to continuous paths formed by the K-samples

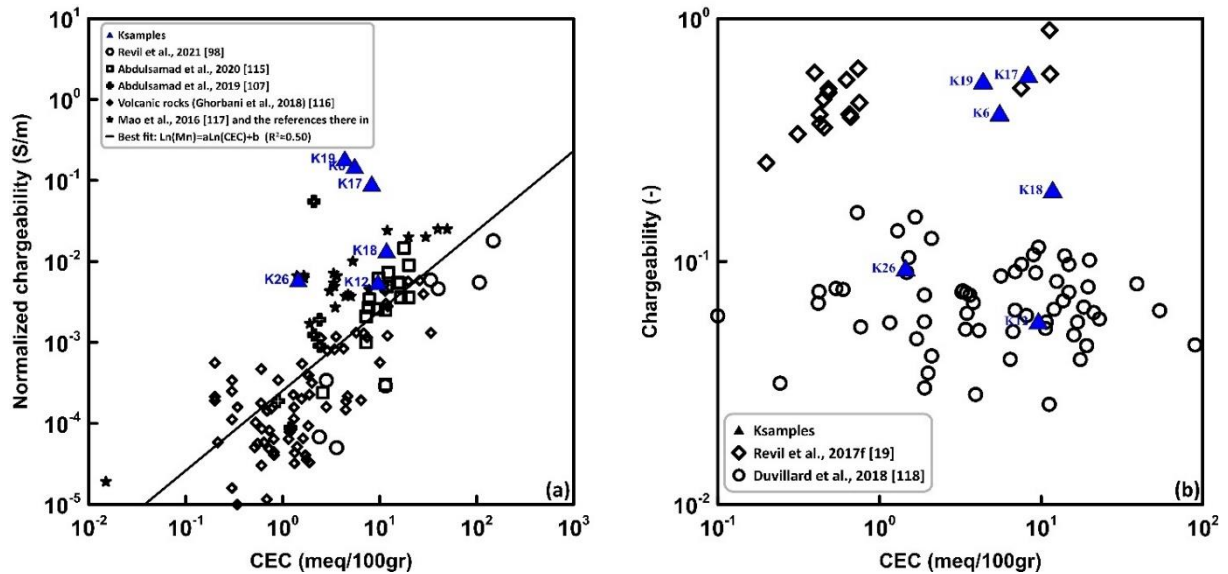metallic minerals content, allowing the electrical current to pass easily.

Fig. 7. a) Normalized chargeability versus CEC. We calculated the K-samples' normalized chargeability through the double Cole-Cole model (M1σ∞). K20 and K23 spectra did not fit well with the Cole-Cole model. We determined normalized chargeability for Abdulsamad et al. (2019) [107] by their reported values for chargeability and instantaneous conductivity. b) There is no relationship between the chargeability and CEC. Duvillard et al.'s data [118] have originated from [55,85,90].
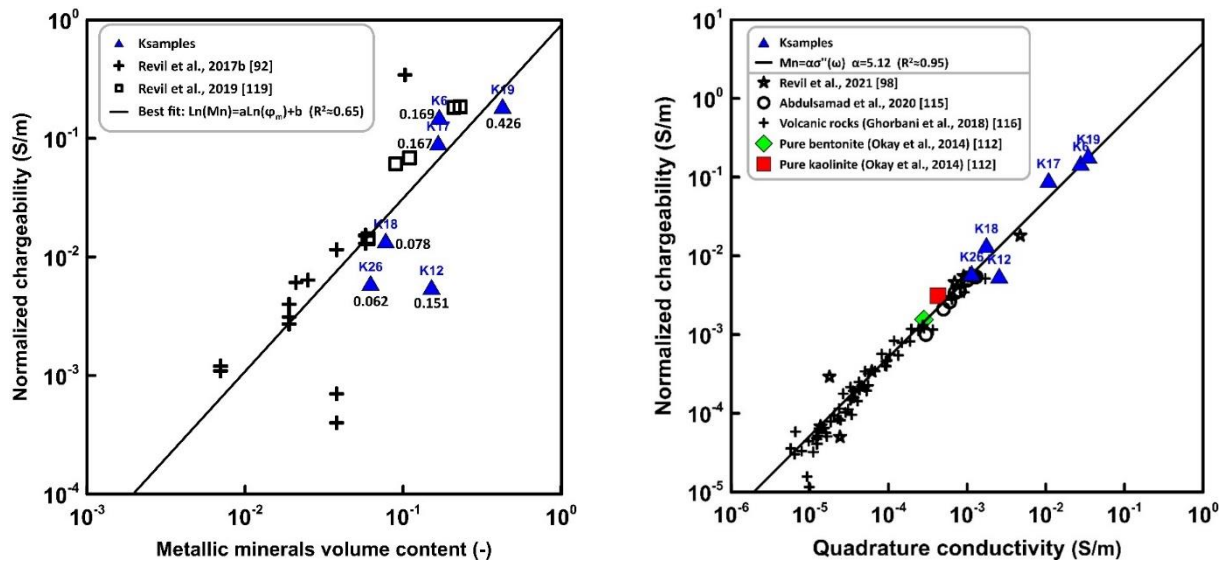

Fig. 8. The linear relationship between the normalized chargeability and the metallic minerals volume content. We calculated the K-samples' normalized chargeability through the double Cole-Cole model (M1σ∞). K20 and K23 spectra did not fit well with the Cole-Cole model. We calculated the literature's normalized chargeability by their reported values for chargeability and instantaneous conductivity.

Fig. 9. The linear relationship between K-samples' normalized chargeability and quadrature conductivity. We calculated the K-samples' normalized chargeability through the double Cole-Cole model (M1σ∞) and their quadrature conductivity at 10 Hz (at a pore-water conductivity of 0.36 S/m). K20 and K23 spectra did not fit well with the Cole-Cole model. K-samples have normalized chargeability and quadrature conductivity higher than ones for pure bentonite and pure kaolinite (95 and 80 percent, respectively).
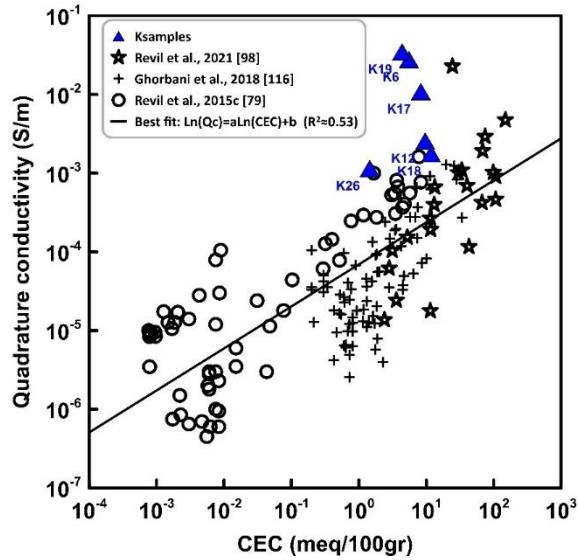
Fig. 10. Quadrature conductivity versus CEC for the K-samples and data from the literature. We took K-samples' quadrature conductivity at 10 Hz (at a pore-water conductivity of 0.36 S/m). We did not display K20 and K23 in this graph due to the lack of their quadrature conductivity at 10 Hz.
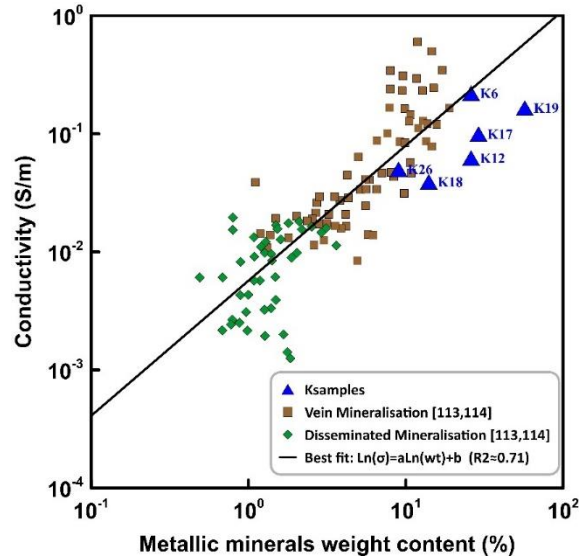

Fig. 12. The linear relationship between conductivity and metallic minerals weight content. We calculated K-samples' conductivity from in-phase and quadrature conductivity at 10 Hz (at a pore-water conductivity of 0.36 S/m). We originate the vein and disseminated mineralization data from [114] and redrawn from [113]. We did not display K20 and K23 in this graph due to the lack of their quadrature conductivity at 10 Hz.
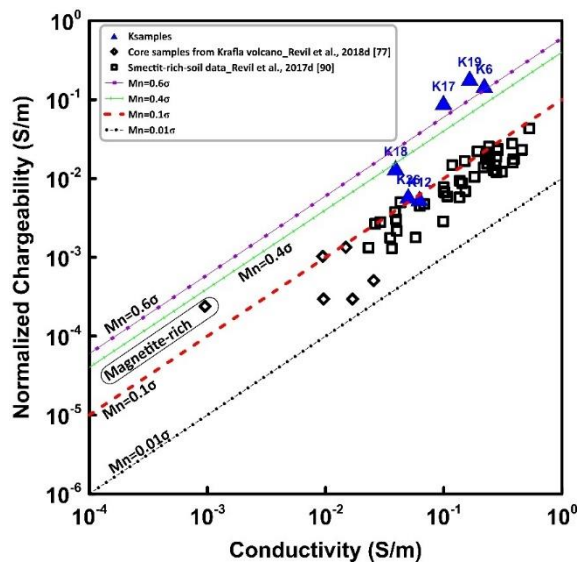
5.2. Chargeability In High-Grade Non-Disseminated Materials

Based on Eq. (16-17), chargeability directly relates to $(9/2)\,\varphi_m$ if the metallic minerals volume content of less than 22% [66]. In addition, there is the known diagram of Pelton et al. (1978), which depicts the relationship between M-φ_m-τ. K-samples are significant because they contain low- to high-grade disseminated and non-disseminated ores. So, we had an excellent opportunity to analyze the M-φ_m relationship of our natural samples using Eq. (17) and Pelton et al.'s diagram. Therefore, we obtained the K-samples' chargeability (M1 in Tables 3 and 4) and extracted the time-constant plots from Pelton et al.'s diagram. Then, we illustrated our samples along with the model of Eq. (17) and time constant plots in Fig. 13. We also showed the samples from [116] and [120] (Table 4) in this figure to gain a more extensive data set. Amongst the literature samples, the ones from [120] are the most similar to ours because they include low- to high-grade disseminated/veined/massive ores.

According to Fig. 13, increasing the metallic volume content (>22%) decreases the chargeability and *increases* the time constant (see also [1,2,5,41,68,113,114,121-122]). Declining chargeability is probably attributed to the decreasing inhomogeneity of the porous media following increasing metallic volume content. Approaching the high-grade samples to the plots with the high time constant is probably due to the

Fig. 11. The linear relationship between the normalized chargeability and conductivity. We calculated K-samples' normalized chargeability through the double Cole-Cole model (M1σ∞) and their conductivity from in-phase and quadrature conductivity at 10 Hz (at a pore-water conductivity of 0.36 S/m). K20 and K23 spectra did not fit well with the Cole-Cole model. The lines Mn=0.4σ and Mn=0.6σ were plotted following the highest amounts of K-samples' chargeability, i.e., 0.59, 0.56, and 0.41 for K17, K19, and K6, respectively.

connection of metallic particles and making the larger particles with the higher time constant.

In other words, there is not a good correlation between Eq. (17) and high-grade samples. So, the coefficients in Eq. (17) are not appropriate to approximate the metallic volume content in high-

grade mineralized rocks. Therefore, to access a better prediction of ore volume content based on chargeability measurements, especially in high-grade materials, it is necessary to import the time constant parameter to the M-φ_m relationship.

Table 4. Metallic minerals volume content and chargeability for K-samples and data from [116,120] are used in Fig. 13. We reported the geometry of the distribution (GoM) for the metallic minerals. We calculated the K-samples chargeability through the double Cole-Cole model. K20 and K23 spectra did not fit well with the Cole-Cole model.

Ghorbani et al. (2018) [116]			Fraser et al. (1964) [120]			K-samples		
φ_m (-)	M (-)	GoM	φ_m (-)	M (-)	GoM	Sample	φ_m (-)	M1 (-) in Table 3
0.000	0.05	DF	0.250	0.27	V, DL	K6	0.169	0.41
0.001	0.08	DF	0.570	0.7	DL,DF,V,M	K12	0.151	0.06
0.002	0.10	DF	0.400	0.45	DL,DF,V	K17	0.167	0.59
0.005	0.09	DF	0.650	0.67	DL,DF,V,M	K18	0.078	0.20
0.008	0.15	DF	0.250	0.48	DL,V,DF	K19	0.426	0.56
0.010	0.17	DF	0.020	0.11	DF	K20	0.533	
0.021	0.16	DF	0.040	0.24	DF	K23	0.130	
0.051	0.43	DF	0.050	0.2	DF	K26	0.062	0.09
0.082	0.43	DF	0.020	0.13	DF, V			
0.103	0.65	DF	0.015	0.09	DF, V			
0.154	0.89	DF	0.041	0.33	DF			
0.206	0.39	DF	0.068	0.35	DF			
0.257	0.57	DF	0.057	0.23	DF			
0.386	0.58	DF	0.878	0.86	DF, M			
			0.018	0.18	DF			
			0.051	0.1	DF			
			0.048	0.15	DF			
			0.013	0.11	DF			

The distribution of metallic minerals is indicated by the following symbols (based on [120]):
V: Veined; DL: Disseminated large blebs; DF: Finely disseminated; M: Massive.
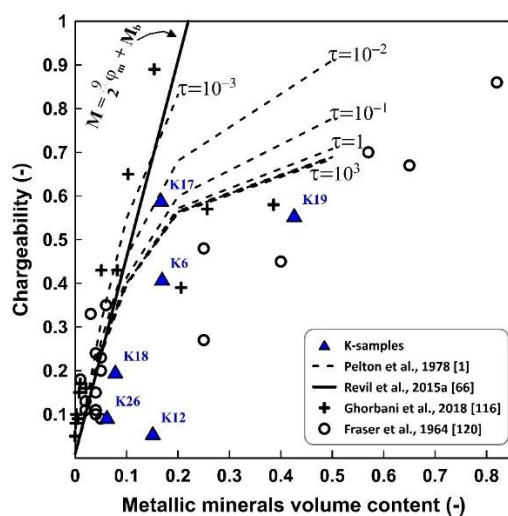
Fig. 13. Chargeability and time constant as a function of metallic minerals volume content for K-samples and data from [116,120]. We extracted time constant plots from [1]. We determined K-samples' chargeability through the double Cole-Cole model and reported them in Tables 3 and 4. K20 and K23 spectra did not fit well with the Cole-Cole model.

6. CONCLUSION

Black shales, as a host rock of sulfide minerals in SEDEX deposits like Koushk, are complex geological environments. Usually, the ores include polarizable pyrite and galena, along with sphalerite. The latter is possible to be polarized. They also contain different amounts of clayey/micaceous materials, organic matter, and insulator grains. In addition, the layered structure of sulfides and clays may cause the electrical parameters to be anisotropic. Therefore, different characteristics and polarization mechanisms in the environments make it challenging to interpret the IP response. Studies like this paper can help to understand these environments and their IP response better.

So, we studied the complex conductivity for samples from Zn-Pb mine Koushk. Our observations showed that chargeability is not affected by CEC and is merely the indicator of the metallic particles volume content. Normalized

chargeability is an IP response affected by metallic particles content besides the CEC and, accordingly, the clays' type and amount. Normalized chargeability and quadrature conductivity have a linear relationship in samples with or without metallic particles. These two parameters in the mineralized samples are higher than the others. Normalized chargeability linearly depends on overall conductivity that, in turn, is controlled by metallic particles volume content. There are different conductivity mechanisms in our samples, with surface conductivity as the dominant one. Afterward, increasing metallic grades decreases the chargeability and increases the time constant. Thus, using a model including chargeability and time constant can be suitable to approximate the metallic particles content from the induced polarization response.

Acknowledgments

Appendix A. Double Cole-Cole Model (Parameters and Inversion)

To determine the polarization of the background (clay/mica) and the polarization of the sulfide minerals, we utilize a double Cole-Cole model in the conductivity form:

$$\sigma^* = \sigma_\infty \left(1 - \frac{M_1}{1+(i\omega\tau_1)^{c_1}} - \frac{M_2}{1+(i\omega\tau_2)^{c_2}}\right) \quad \text{(A-1)}$$

where σ^* is the complex conductivity, σ_∞ denotes the instantaneous conductivity, M1 and M2 are the chargeabilities related to low- and high-frequency polarization, ω is the angular frequency, τ_1 and τ_2 are the time constants, and c1 and c2 denote the Cole-Cole exponents (dimensionless).

The first Cole-Cole model represents the polarization of low-frequency dispersion (index 1). The second one corresponds to high-frequency dispersion (index 2), i.e., the Maxwell-Wagner polarization or the EM coupling [83].

The instantaneous and DC conductivity (σ_0) are written as:

$$\sigma_\infty = \sigma_1^\infty + \sigma_2^\infty \quad \text{(A-2)}$$

$$\sigma_0 = \sigma_1^0 + \sigma_2^0 \quad \text{(A-3)}$$

Based on the continuity condition on the conductivity:

$$\sigma_1^\infty = \sigma_2^0 \quad \text{(A-4)}$$

M1 and M2 are determined as:

$$M_1 = \frac{\sigma_1^\infty - \sigma_1^0}{\sigma_\infty} \quad \text{(A-5)}$$

$$M_2 = \frac{\sigma_2^\infty - \sigma_2^0}{\sigma_\infty} \quad \text{(A-6)}$$

The chargeability, in general, is defined by $M = (\sigma_\infty - \sigma_0)/\sigma_\infty$, so, the equation $M = M_1 + M_2$ is valid and due to $0 \leq M \leq 1$, we have $0 \leq M_1 + M_2 \leq 1$. σ_1^∞ and σ_2^∞ can be obtained from:

$$\sigma_1^\infty = \frac{1}{2}\sigma_\infty(1-M_2) \quad \text{(A-7)}$$

$$\sigma_2^\infty = \frac{1}{2}\sigma_\infty(1+M_2) \quad \text{(A-8)}$$

To invert the complex conductivity spectra using the double Cole-Cole model, we use the nonlinear iterative method based on a Monte Carlo Markov Chain sampling algorithm [123]. The Bayesian method describes available prior information on the model vector, using a probability density $P(\vec{m})$. $\vec{m}$ is the model vector of unknown parameters $\vec{m} = [\log(\sigma_\infty), M_1, c_1, \log(\tau_1), M_1, c_2, \log(\tau_2)]$. Then, the algorithm combines this information with the observed data vector $\vec{d}_{obs}$ and the provided information by the Cole-Cole model (Eq. A-1) $L(\vec{m})$. In Bayesian theory, the posterior probability density $\sigma(\vec{m})$ equals the product of the prior probability density $P(\vec{m})$ and a likelihood function $L(\vec{m})$ (Eq. A-9). $\sigma(\vec{m})$ measures the fit between the observed data and data provided by the model $\vec{m}$.

$$\sigma(\vec{m}) = kP(\vec{m})L(\vec{m}) \quad \text{(A-9)}$$

where k is a normalization constant. We display the results of the complex conductivity by a vector of the observed data ($\vec{d}_{obs}$) with Gaussian experimental uncertainties. We utilize the independent identical Gaussian uncertainties distribution. Then, the likelihood function that characterizes the experimental uncertainties is calculated by the following Equation:

$$L(\vec{m}) = k\exp(-S(\vec{m})/s^2) \quad \text{(A-10)}$$

where s^2 is the total noise variance, and $S(\vec{m})$ is the misfit function defined as:

$$S(\vec{m}) = \frac{1}{2}\sum_{i=1}^{n}(g^{i}(\vec{m}) - d_{obs}^{i})^2 \qquad \text{(A-11)}$$

where $\vec{d}$ is the data vector and $g(\vec{m}) = \sigma^*$ is the forward-modelling function. The acceptance probability for a model is determined by:

$$P_{accept} = \begin{cases} 1 & \text{if } S(\vec{m}_{new}) \leq S(\vec{m}_{old}) \\ \exp(-\Delta S/s^2) & \text{if } S(\vec{m}_{new}) > S(\vec{m}_{old}) \end{cases} \qquad \text{(A-12)}$$

where $\Delta S = S(\vec{m}_{new}) - S(\vec{m}_{old})$. The observed data in this inversion process are the real and imaginary parts of the complex conductivity calculated from the amplitude and phase measured at different frequencies. We consider the standard deviation (s) of 10% of the measured complex conductivity values related to the maximum experimental error [83]. Locally, uniform law is valid for describing the prior probability density on the model parameters. The law states that the probability distribution is constant over the interval $[\theta_1, \theta_2]$ and vanishes in the other distances. To obtain the Cole-Cole parameters, Jeffrey's parameters can be used for the inversion to satisfy the intervals conditions as $0 \leq (M_1, M_2, c_1, c_2) \leq 1$ and $\sigma_\infty > 0$ [124]. Ultimately, we calculate the root-mean-square error (rms) as a criterion to qualify the quality of the fit, as:

$$rms^2 = \frac{1}{n}\sum_{i=1}^{n}\left(\frac{g^{i}(\vec{m}) - d_{obs}^{i}}{d_{obs}^{i}}\right)^2 \qquad \text{(A-13)}$$

where n is the number of measurements.

REFERENCES

[1]	Pelton, W.H., Ward, S.H., Hallof, P.G., Sill, W.R. and Nelson, P.H. (1978). Mineral Discrimination and removal of inductive coupling with multifrequency IP. Geophysics. 43(3): 588-609.

[2]	Vanhala, H. (1997). Laboratory and field studies of environmental and exploration applications of the spectral induced-polarization (SIP) method: Ph.D. Dissertation, Helsinki University of Technology, Espoo, Finland.

[3]	Bérubé, C.L., Chouteau, M., Olivo, G.R., Perrouty, S., Shamsipour, P. and Enkin, R.J. (2017). Spectral induced polarization signatures of altered metasedimentary rocks from the Canadian malartic gold deposit Bravo zone, Quebec, Canada: SAGEEP, Denver, Colorado, USA.

[4]	Mostafaei, K. and Ramazi, H. (2019). Investigating the applicability of induced polarization method in ore modeling and drilling optimization: a case study from Abassabad, Iran. Near Surface Geophysics, 17(6): 637-652.

[5]	Revil, A., Vaudelet, P., Su, Z. and Chen, R. (2022). Induced Polarization as a tool to Assess Mineral Deposits: A Review. Minerals. 12(5): 571.

[6]	Börner, F., Gruhne, M. and Schön, J. (1993). Contamination indications derived from electrical properties in the low-frequency range. Geophysical Prospecting. 41(1): 83-98.

[7]	Grimm, R.E., Olhoeft, R., McKinley, K., Rossabi, J. and Riha, B. (2005). Nonlinear complex resistivity survey for DNAPL at the Savannah river site A-014 outfall. Journal of Environmental & Engineering Geophysics. 10(4): 351-364.

[8]	Deng, Y., Shi, X., Revil, A., Wu, J. and Ghorbani, A. (2018). Complex conductivity of oil-contaminated clayey soils. Journal of Hydrology, 561(1): 930-942.

[9]	Ntarlagiannis, D., Williams, K.H., Slater, L. and Hubbard, S.S. (2005). Low-frequency electrical response to microbial induced sulfide precipitation. Journal of Geophysical Research. 110(G2): G02009.

[10]	Chen, J., Hubbard, S.S., Williams, K.H., Flores-Orozco, A. and Kemna, A. (2012). Estimating the spatiotemporal distribution of geochemical parameters associated with biostimulation using spectral induced polarization data and hierarchical Bayesian models. Water Resources Research, 48(5): W0555.

[11]	Flores-Orozco, A., Kemna, A., Oberdörster, C., Zschornack, L., Leven, C., Dietrich, P. and Weiss, H. (2012b). Delineation of subsurface hydrocarbon contamination at a former hydrogenation plant using spectral induced polarization imaging. Journal of Contaminant Hydrology. 136-137: 131–144.

[12]	Mewafy, F.M., Werkema, D.D., Jr., Atekwana, E.A., Slater, L.D., Aal, G.A., Revil, A. and Ntarlagiannis, D. (2013). Evidence that bio-metallic mineral precipitation enhances the complex conductivity response at a hydrocarbon contaminated site. Journal of Applied Geophysics. 98: 113–123.

[13]	Ntarlagiannis, D., Doherty, R. and Williams, K.H. (2010). Spectral induced polarization signatures of abiotic FeS precipitation. Geophysics. 75(4): F127–F133.

[14]	Abdel Aal, G.Z., Atekwana, E.A. and Revil, A. (2014). Geophysical signatures of disseminated iron minerals: A proxy for understanding subsurface biophysicochemical processes. Journal of Geophysical Research: Biogeosciences. 119(9): 1831–1849.

[15]	Placencia-Gómez, E., Pamainen, A., Slater, L. and Leveinen, J. (2015). Spectral induced polarization (SIP) response of mine tailings. Journal of Contaminant Hydrology. 173C: 8-24.

[16]	Placencia-Gómez, E. (2015). Spectral induced polarization investigations in presence of metal sulphide minerals: implications for monitoring the generation of acid mine drainage. Doctoral dissertation. Helsinki, Finland.

[17]	Okay, G., Cosenza, P., Ghorbani, A., Camerlynck, C., Cabrera, J., Florsch, N. and Revil, A. (2013). Characterization of macroscopic heterogeneities in

clay-rocks using induced polarization: Field tests at the experimental underground research laboratory of Tournemire (Aveyron, France). Geophysics Prospecting. 61(1): 134–152.

[18]   Revil, A., Le Breton, M., Niu, Q., Wallin, E., Haskins, E. and Thomas, D.M. (2017e). Induced polarization of volcanic rocks- 1. Surface versus quadrature conductivity. Geophysical Journal International. 208(2): 826-844.

[19]   Revil, A., Le Breton, M., Niu, Q., Wallin, E., Haskins, E. and Thomas, D.M. (2017f). Induced polarization of volcanic rocks. 2. Influence of pore size and permeability. Geophysical Journal International. 208(2): 814-825.

[20]   Revil, A. and Gresse, M. (2021). Induced Polarization as a tool to assess alteration in geothermal systems: a review. Minerals. 11(962).

[21]   Leroy, P., Hördt, A., Gaboreau, S., Zimmermann, E., Claret, F., Bücker, M., Stebner, H., Huisman, J.A. (2019). Spectral induced polarization of low-pH cement and concrete. Cement and Concrete Composites, 104, 103397.

[22]   Bate, B., Cao, J., Zhang, C., Hao, N., Wang, S. (2021). Monitoring lime and cement improvement using spectral induced polarization and bender element techniques. Journal of Rock Mechanics and Geotechnical Engineering, 13(1), 202-211.

[23]   Jia, J., Ke, S., Rezaee, R., Yin, C., Chen, S. and Zhong, Z. (2022). Time-domain induced polarization response and cementation index estimation of synthetic sandstones. Arabian Journal of Geosciences. 15(17), 1429.

[24]   Kiberu, J. (2002). Induced polarization and Resistivity measurements on a suite of near surface soil samples and their empirical relationship to selected measured engineering parameters. International Institute for Geo-information Science and Earth Observation. M.Sc. Thesis, Netherlands.

[25]   Clavier, C., Heim, A. and Scala, C. (1976). Effect of pyrite on resistivity and other logging measurements. In Proceedings of the SPWLA 17th Annual Logging Symposium, Denver, CO, USA, 9 June 1976.

[26]   Sternberg, B.K. (1991). A review of some experience with the induced-polarization/resistivity method for hydrocarbon surveys: Successes and limitations. Geophysics. 56(10): 1522–1532.

[27]   Veeken, P.C., Legeydo, P.J., Davidenko, Y.A., Kudryavceva, E.O., Ivanov, S.A. and Chuvaev, A. (2009). Benefits of the induced polarization geoelectric method to hydrocarbon exploration. Geophysics. 74(2): B47–B59.

[28]   Flekkøy, E.G., Legeydo, P., Håland, E., Drivenes, G. and Kjerstad, J. (2013). Hydrocarbon detection through induced polarization: Case study from the Frigg area. In SEG Technical Program Expanded Abstracts. The Society of Exploration Geophysicists, Houston, TX, USA.

[29]   Börner, F.D. and Schön, J.H. (1991). A relation between the quadrature component of electrical conductivity and the specific surface area of sedimentary rocks. The Log Analyst. 32(05): 612-613.

[30]   Glover, P.W.J., Gomez, J.B., Meredith, P.G., Hayashi, K, Sammonds, P.R. and Murrell, S.A.F. (1997). Damage of saturated rocks undergoing triaxial deformation using complex electrical conductivity measurements: experimental results. Physics and Chemistry of the Earth. 22(1-2): 57-61.

[31]   Glover, P.W.J., Gomez, J.B. and Meredith, P.G. (2000). Fracturing in saturated rocks undergoing triaxial deformation using complex electrical conductivity measurements: experimental study. Earth and Planetary Sciences Letters. 183(1-2): 201-213.

[32]   Slater, L. and Lesmes, D. (2002a). Electrical-hydraulic relationships were observed for unconsolidated sediments. Water Resources Research. 38(10): 1213.

[33]   Kemna, A., Binley, A. and Slater, L. (2004) Crosshole IP imaging for engineering and environmental applications. Geophysics, 69(1): 97-107.

[34]   Titov, K., Kemna, A. Tarasov, A. and Vereecken, H. (2004). Induced polarization of unsaturated sands determined through time domain measurements. Vadose Zone Journal. 3(4): 1160-1168.

[35]   Ulrich, C. and Slater, L.D. (2004). Induced polarization measurements on unsaturated, unconsolidated sands. Geophysics. 69(3): 762–771.

[36]   Binley, A., Slater, L., Fukes, M. and Cassiani, G. (2005). The relationship between spectral induced polarization and hydraulic properties of saturated and unsaturated sandstone. Water Resources Research, 41(12): W12417.

[37]   Tarasov, A. and Titov, K. (2007). Relaxation time distribution from time domain induced polarization measurements. Geophysical Journal International. 170(1): 31-43.

[38]   Vaudelet, P., Revil, A., Schmutz, M., Franceschi, M. and Bégassat, P. (2011). Changes in induced polarization associated with the sorption of sodium, lead, and zinc on silica sands. Journal of Colloid and Interface Science. 360(2): 739–752.

[39]   Leroy, P. and Revil, A. (2004). A triple-layer model of the surface electrochemical properties of clay minerals. Journal of Colloid and Interface Science. 270(2): 371–380.

[40]   Revil, A., Leroy, P. and Titov, K. (2005). Characterization of transport properties of argillaceous sediments: Application to the Callovo-Oxfordian argillite. Journal of Geophysical Research. 110(B6).

[41]   Vacquier, V., Holmes, C.R., Kintzinger, P.R. and LaVergne, M. (1957). Prospecting for groundwater by induced electrical polarization. Geophysics. 22(3): 660-687.

[42]   Weller, A. and Börner, F.D. (1996). Measurements of spectral induced polarization for

environmental purposes. Environmental Geology. 27: 329–334.

[43]   Cole, K.S. and Cole, R.H. (1941). Dispersion and absorption in dielectrics, I. Alternating current characteristics. Journal of Chemical Physics. 9(4): 341-351.

[44]   Jonscher, A.K. (1983). Dielectric relaxation in solids. Chelsea Dielectrics Press Ltd., London.

[45]   Wait, J.R. (1984). Relaxation time phenomena and induced polarization. Geoexploration. 22(2): 107-127.

[46]   Schwarz, G. (1962). A theory of the low-frequency dielectric dispersion of colloidal particles in electrolyte solution. The Journal of Physical Chemistry. 66(12): 2636-2642.

[47]   Schurr, J. M. (1964). On the theory of the dielectric dispersion of spherical colloidal particles in electrolyte solution. The Journal of Physical Chemistry. 68(9): 2407-2413.

[48]   Marshall, D.J. and Madden, T.R. (1959). Induced polarization, a study of its causes. Geophysics. 24(4): 790-816.

[49]   Wong, J. (1979). An electrochemical model of the induced-polarization phenomenon in disseminated sulfide ores. Geophysics. 44(7): 1245-1265.

[50]   Maxwell, J.C. (1892). A Treatise on Electricity and Magnetism. 3rd Ed., Oxford University Press, London.

[51]   Dukhin, S.S. and Shilov, P. (1974). Dielectric phenomena and the double layer in disperse systems and polyelectrolytes. John Wiley and Sons, Inc., New York.

[52]   Fixman, M. (1980). Charged macromolecules in external fields, I. The sphere. Journal of Physical Chemistry. 72(1): 5177-5186.

[53]   Sen, P.N., Scala, C. and Cohen, M.H. (1981). A self-similar model for sedimentary rocks with application to the dielectric constant of fused glass beads. Geophysics. 46(5): 781-795.

[54]   Lyklema, J., Dukhin, S.S. and Shilov, V.N. (1983). The relaxation of the double layer around colloidal particles and the low-frequency dielectric dispersion: Part I. Theoretical considerations. Journal of Electroanalytical Chemistry and Interfacial Electrochemistry. 143(1-2): 1-21.

[55]   Vinegar, H.J. and Waxman, M.H. (1984). Induced polarization of shaly sands. Geophysics. 49(8): 1267-1287.

[56]   Wagner, K.W. (1914). Erklärung der dielektrischen Nachwirkungsvorgänge auf Grund Maxwellscher Vorstellungen. Archiwum Elektrotechniki (Archives of Electrical Engineering (AEE)). 2(9): 371-387.

[57]   Bruggeman, D.A.G. (1935). Berechung verschieder physikalischer konstanten von heterogenen substranzen. Annals of Physics. 24: 639-679.

[58]   Hanai, T. (1968). Electrical properties of emulsions. in: Emulsions Science, (Sherman, P. (Ed.)), Academic Press, San Diego, Calif, 354-477.

[59]   De Lima, O.A.L. and Sharma, M.M. (1992). A generalized Maxwell-Wagner theory for membrane polarization in shaly sands. Geophysics. 57(3): 431-440.

[60]   Shilov, V.N., Delgado, A.V., Gonzalez-Caballero, F. and Grosse, C. (2001). Thin double layer theory of the wide-frequency range dielectric dispersion of suspensions of non-conducting spherical particles including surface conductivity of the stagnant layer. Colloids and Surfaces A: Physicochemical and Engineering Aspects. 192(1-3): 253-265.

[61]   Lesmes, D.P. and Morgan, F.D. (2001). Dielectric spectroscopy of sedimentary rocks. Journal of Geophysical Research (JGR). 106(D10): 13392-13346.

[62]   Leroy, P., Revil, A., Kemna, A., Cosenza, P. and Ghorbani, A. (2008). Complex conductivity of water-saturated packs of glass beads. Journal of Colloid and Interface Science. 321(1):103-117.

[63]   Cosenza, P., Ghorbani, A., Revil, A., Zamora, M., Schmutz, M., Jougnot, D. and Florsch, N. (2008). A physical model of the low-frequency electrical polarization of clay-rocks. Journal of Geophysical Research (JGR). 113: B08204.

[64]   Leroy, P. and Revil, A. (2009). A mechanistic model for the spectral induced polarization of clay materials. Journal of Geophysical Research (JGR). 114(B10202).

[65]   Revil, A. and Florsch, N. (2010). Determination of permeability from spectral induced polarization in granular media. Geophysical Journal International. 181(3): 1480-1498.

[66]   Revil, A., Florsch, N. and Mao, D. (2015a). Induced polarization response of porous media with metallic particles- Part 1: A theory for disseminated semiconductors. Geophysics. 80(5): D525-D538.013.

[67]   Misra, S., Torres-Verdín, C., Revil, A., Rasmus, J. and Homan, D. (2016). Interfacial polarization of disseminated conductive minerals in absence of redox-active species-Part 1: Mechanistic model and validation. Geophysics. 81(2): E139-E157.

[68]   Abdulsamad, F., Florsch, N. and Camerlynck, C. (2017). Spectral induced polarization in a sandy medium containing semiconductor materials: experimental results and numerical modelling of the polarization mechanism. Near Surface Geophysics. 15(6): 669-683.

[69]   Schlumberger, C. (1920). Study of underground electrical prospecting: Paris.

[70]   Rajabi, A.R. (2008). Geology, mineralogy, texture, and structure, geochemistry and genesis of Chahmir Zn-Pb deposit, south of Behabad, Yazd Province. Tehran, Tarbiat Modares University, 245 p.

[71]   Rajabi, A.R., Rastad, E., Rashidnejed Omran, N. and Mohammadi Niaei, R. (2008). Chahmir deposit: A sedimentary-exhalative Zn-Pb deposit in Bafq basin, Central Iran. 33rd International Geology Congress, Oslo, Norway, Abstract.

[72]   Yaghubpur, A., and Mehrabi, B., 1997, Kushk zinc-lead deposit: a typical black-shale-hosted deposit in Yazd State, Iran. Journal of Sciences, 8(2), 117–125.

[73]   Rajabi, A.R., Rastad, E., Alfonso, P. and Canet, C. (2012). Geology, ore facies and sulphur isotopes of the Koushk vent-proximal sedimentary-exhalative deposit, Posht- e-Badam Block, Central Iran. International Geology Review. 54(14): 1635-1648.

[74]   Nelson, D.W. and Sommers, L.E. (1996). Total carbon, organic carbon, and organic matter. In Sparks, D.L., et al., Eds., Methods of soil analysis. Part 3, SSSA book series, Madison, 961-1010.

[75]   Środoń, J. and McCarty, D.K. (2008). Surface area and layer charge of smectite from CEC and EGME/H2O-retention measurements. Clays and Clay Minerals. 56(2): 155-174.

[76]   Derkowski, A. and Bristow, T. (2012). On the problems of total specific surface area and cation exchange capacity measurements in organic-rich sedimentary rocks. Clays and Clay Minerals. 60(4): 348-362.

[77]   Revil, A., Qi, Y., Ghorbani, A., Soueid Ahmed, A., Ricci, T. and Labazuy, P. (2018d). Electrical conductivity and induced polarization investigations at Krafla volcano, Iceland. Journal of Volcanology and Geothermal Research. 368: 73–90.

[78]   Ciesielski, H. and Sterckeman, T. (1997). Determination of cation exchange capacity and exchangeable cations in soils by means of cobalt hexamine trichloride. Effects of experimental conditions: Agronomie: Agriculture and Environment, 17: 1-7.

[79]   Revil, A., Binley, A., Mejus, L. and Kessouri, P. (2015c). Predicting permeability from the characteristic relaxation time and intrinsic formation factor of complex conductivity spectra. Water Resources Research. 51(8): 6672-6700.

[80]   Aran, D., Maul, A., Masfaraud, J.F. (2008). A spectrophotometric measurement of soil cation exchange capacity based on cobaltihexamine chloride absorbance. Surface geosciences (pedology), 340(12): 865-871.

[81]   Revil, A., Hermitte, D., Spangenberg, E. and Cocheme, J.J. (2002). Electrical properties of zeolitized volcaniclastic materials, Journal of Geophysical Research, 107(B8): 2168.

[82]   Revil, A., Coperey, A., Mao, D., Abdulsamad, F., Ghorbani, A., Rossi, M. and Gasquet, D. (2018c). Induced polarization response of porous media with metallic particles- Part 8: Influence of temperature and salinity. Geophysics. 83(6): E435-E456.

[83]   Qi, Y., Soueid Ahmed, A., Revil, A., Ghorbani, A., Abdulsamad, F., Florsch, N. and Bonnenfant, J. (2018). Induced polarization response of porous media with metallic particles- Part 7: Detection and quantification of buried slag heaps. Geophysics. 83(5): E277–E291.

[84]   Zimmermann, E., Kemna, A., Berwix, J., Glaas, W., Munch, H. and Huisman, J. (2008). A high accuracy impedance spectrometer for measuring sediments with low polarizability. Measurement Science and Technology. 19(10): 105603.

[85]   Revil, A., Coperey, A., Deng, Y., Cerepi, A. and Seleznev, N. (2018a). Complex conductivity of tight sandstones. Geophysics. 83(2): E55-E74.

[86]   Ahmadi, S., Coperey, A., Ghorbani, A. and Revil, A. (2022). Anisotropy of induced polarization response-sulfide ore samples. 6th International Meeting on Induced Polarization. April 6th, 2022, Annecy (Haute-Savoie), France.

[87]   Bücker, M.b. (2018). Pore-scale modelling of induced-polarization mechanisms in geologic materials. Doctoral Dissertation. University of Bonn, Bonn, Germany.

[88]   Revil, A., Kessouri, P. and Torres-Verdín, C. (2014). Electrical conductivity, induced polarization, and permeability of the Fontainebleau sandstone. Geophysics. 79(5): D301-D318.

[89]   Seigel, H.O. (1959). Mathematical formulation and type curves for induced polarization. Geophysics, 24(3): 547-565.

[90]   Revil, A., Coperey, A., Shao, Z., Shao, Z., Florsch, N., Fabricius, I.L., Deng, Y., Deng, Y., Delsman, J.R., Pauw, P.S., Karaoulis, M., Louw, P.G., Baaren, E.S., Dabekaussen, W., Menkovic, A. and Gunnink, J.L. (2017d). Complex conductivity of soils. Water Resources Research. 53(8): 7121-7147.

[91]   Revil, A., Abdel Aal, G.Z., Atekwana, E.A., Mao, D. and Florsch, N. (2015b). Induced polarization response of porous media with metallic particles-Part 2: Comparison with a broad database of experimental data. Geophysics. 80(5): D539-D552.

[92]   Revil, A., Mao, D., Shao, Z., Sleevi, M.F. and Wang, D. (2017b). Induced polarization response of porous media with metallic particles- Part 6: The case of metals and semimetals. Geophysics. 82(2): E97-E110.

[93]   Revil, A. (2012). Spectral induced polarization of shaly sands: Influence of the electrical double layer. Water Resources Research. 48(2): W02517.

[94]   Revil, A. (2013a). On charge accumulation in heterogeneous porous rocks under the influence of an external electrical field. Geophysics. 78(4): D271–D291.

[95]   Revil, A., Tartrat, T., Abdulsamad, F., Ghorbani, A. and Coperey, A. (2018b). Chargeability of porous rocks with or without metallic particles. Petrophysics, 59(4): 544-553.

[96]   Revil, A., Ghorbani, A., Gailler, L.S., Gresse, M., Cluzel, N., Panwar, N., and Sharma, R. (2018f). Electrical conductivity and induced polarization investigations at Kilauea volcano, Hawai'i. Journal of Volcanology and Geothermal Research, 368(15): 31-50.

[97] Tartrat, T., Revil, A., Abdulsamad, F., Ghorbani, A., Jougnot, D., Coperey, A., Yven, B. and Vaissière, R. (2019). Induced polarization response of porous media with metallic particles- Part 10: Influence of desiccation. Geophysics, 84(5): E357-E375.

[98] Revil, A., Qi, Y., Ghorbani, A., Gresse, M. and Thomas, D.M. (2021). Induced polarization of volcanic rocks. 5. Imaging the temperature field of shield volcanoes. Geophysical Journal International, Oxford University Press (OUP), 225: 1492-1509.

[99] Revil, A., Ghorbani, A., Jougnot, D., and Yven, B. (2023). Induced polarization of clay-rich materials- Part 1: The effect of desiccation: Geophysics, 88(4): 1–16.

[100] Major, J. and Silic, J. (1981). Restrictions on the use of Cole-Cole dispersion models in complex resistivity interpretation. Geophysics, 46: 916–931.

[101] Tarasov, A., and Titov, K. (2013). On the use of the Cole-Cole equations in spectral induced polarization. Geophysical Journal International. 195(1): 352–356.

[102] Breede, K., Kemna, A., Esser, O., Zimmermann, E., Vereecken, H. and Huisman, J.A. (2012). Spectral induced polarization measurements on variably saturated sand-clay mixtures. Near Surface Geophysics, 10(6): 479-489.

[103] Kemna, A., Binley, A., Cassiani, G., Niederleithinger, E., Revil, A., Slater, L.D., Williams, K.H., Flores-Orozco, A., Haegel, F.H., Hördt, A., Kruschwitz, S., Leroux, V., Titov, K. and Zimmermann, E. (2012). An overview of the spectral induced polarization method for near-surface applications. Near Surface Geophysics. 10(6): 453-468.

[104] Niu, Q., Prasad, M., Revil, A. and Saidian, M. (2016). Textural control on the quadrature conductivity of porous media. Geophysics. 81(5): E297-E309.

[105] Wang, C. and Slater, L.D. (2019). Extending accurate spectral induced polarization measurements into the kHz range: modelling and removal of errors from interactions between the parasitic capacitive coupling and the sample holder. Geophysical Journal International. 218(2): 895-912.

[106] Flores-Orozco, A., Kemna, A. and Zimmermann, E. (2012a). Data error quantification in spectral induced polarization imaging. Geophysics. 77(3): E227-E237.

[107] Abdulsamad, F., Revil, A., Ghorbani, A., Toy, V., Kirilova, M., Coperey, A., Duvillard, P.A., Ménard, G. and Ravanel, L. (2019). Complex Conductivity of Graphitic Schists and Sandstones. Journal of Geophysical Research: Solid Earth. 124(8): 8223-8249.

[108] Meimaroglou, N. and Mouzakis, C. (2019). Cation Exchange Capacity (CEC), texture, consistency and organic matter in soil assessment for earth construction: The case of earth mortars. Construction and Building Materials. 221(3): 27–39.

[109] Revil, A. (2013b). Effective conductivity and permittivity of unsaturated porous materials in the frequency range 1 mHz-1GHz. Water Resources Research. 49(1): 306-327.

[110] Revil, A., Sleevi, M.F. and Mao, D. (2017a). Induced polarization response of porous media with metallic particles-Part 5: Influence of the background polarization. Geophysics. 82(2): E77–E96.

[111] Revil, A., Murugesu, M., Prasad, M. and Le Breton, M. (2017c). Alteration of volcanic rocks: a new non-intrusive indicator based on induced polarization measurements. Journal of Volcanology and Geothermal Research. 341(C): 351-362.

[112] Okay, G., Leroy, P., Ghorbani, A., Cosenza, P., Camerlynck, C., Cabrera, J., Florsch, N. and Revil, A. (2014). Spectral induced polarization of clay-sand mixtures: Experiments and modeling. Geophysics. 79(6): E353–E375.

[113] Nelson, P.H. and Van Voorhis, G.D. (1983). Estimation of sulfide content from induced polarization data. Geophysics. 48(1): 62-75.

[114] Dentith, M. and Mudge, S.T. (2014). Geophysics for the mineral exploration geoscientist. Cambridge University Press, New York, ISBN 978-0-521-80951-1 Hardback.

[115] Abdulsamad, F., Revil, A., Prime, N., Gnonnoue, P.Y., Plé, O. and Schmutz, M. (2020). Complex conductivity of rammed earth. Engineering Geology, Elsevier, 273.

[116] Ghorbani, A., Revil, A., Coperey, A., Soueid Ahmed, A., Roque, S., Heap, M.J., Grandis, H. and Viveiros, F. (2018). Complex conductivity of volcanic rocks and the geophysical mapping of alteration in volcanoes. Journal of Volcanology and Geothermal Research. 357: 106-127.

[117] Mao, D., Revil, A. and Hinton, J. (2016). Induced polarization response of porous media with metallic particles- Part 4: Detection of metallic and nonmetallic targets in time-domain-induced polarization tomography. Geophysics. 81(4): D345–D361.

[118] Duvillard, P.A., Revil, A., Qi, Y., Soueid Ahmed, A., Coperey, A. and Ravanel, L. (2018). Three-Dimensional Electrical Conductivity and Induced Polarization Tomography of a Rock Glacier. Journal of Geophysical Research: Solid Earth. 123(11): 9528-9554.

[119] Revil, A., Razdan, M., Julien, S., Coperey, A., Abdulsamad, F., Ghorbani, A., Gasquet, D., Sharma, R. and Rossi, M. (2019). Induced polarization response of porous media with metallic particles-Part 9. Influence of permafrost. Geophysics. 84(5): E337-E355.

[120] Fraser, D.C., Keevil, N.B. and Ward, S.H. (1964). Conductivity spectra of rocks from the Craigmont ore environment. Geophysics. XXIX(5), 832-847.

[121] Revil, A. and Cosenza, P. (2010). Discussion and reply comment on "Generalized effective-medium theory of induced polarization, Michael Zhdanov, 2008, Geophysics, 73, F197–F211". Geophysics. 75(2): X7–X9

[122]   Martin, T. and Weller, A. (2023). Superposition of induced polarization signals measured on pyrite–sand mixtures. Geophysics Journal International. 234(1): 699–711.

[123]   Mosegaard, K. and Tarantola, A. (1995). Monte Carlo sampling of solutions to inverse problems. Journal of Geophysical Research. 100(B7): 12431–12447.

[124]   Ghorbani, A., Camerlynck, C., Florsch, N., Cosenza, P., Tabbagh, A. and Revil, A. (2007). Bayesian inference of the Cole-Cole parameters from time and frequency-domain induced polarization. Geophysical Prospecting. 55(4): 589–605.